

The dynamics of a fully radiative rapidly rotating star

F. Espinosa Lara and M. Rieutord

Laboratoire d'Astrophysique de Toulouse et Tarbes, UMR 5572, CNRS et Université Paul Sabatier Toulouse 3, 14 avenue E. Belin, 31400 Toulouse, France

May 26, 2019

ABSTRACT

Context. Recent results of interferometry and asteroseismology require more and more precise models of rapidly rotating stars.

Aims. We describe the basic structure and the hydrodynamics of a fully radiative star as a preliminary step towards more realistic models of rotating stars.

Methods. We consider a solar mass of perfect gas enclosed in a spherical container. The gas is self-gravitating and rotating; it is the seat of nuclear heating and heat diffusion is due to radiative diffusion with Kramers type opacities. Equations are solved numerically with spectral methods in two dimensions with a radial Gauss-Lobatto grid and spherical harmonics.

Results. We compute the centrifugally flattened structure of such a star; the von Zeipel model, which says that the energy flux is proportional to the local effective gravity is tested: we show that it overestimates by almost a factor 2 the ratio of the polar to the equatorial energy flux. We determine also the Brunt-Väisälä frequency distribution and show that outer equatorial regions in a radiative zone are convectively unstable when the rotation is fast enough. We compute the differential rotation and meridional circulation stemming from the baroclinicity of the star and show that, in such radiative zones, equatorial regions rotate faster than polar ones. The surface differential rotation is also shown to reach a universal profile when rotation is slow enough (less than 36% of the breakup one), viscosity and Prandtl number being small.

Key words. Hydrodynamics – stars: rotation

1. Introduction

Recent observations of nearby stars with optical or infrared interferometers have open a new window on rapidly rotating stars. The work of Domiciano de Souza et al. (2005), Zorec et al. (2005), McAlister et al. (2005), Peterson et al. (2006a), Peterson et al. (2006b), Kervella & Domiciano de Souza (2006), Aufdenberg et al. (2006) show that observational techniques are now able to constrain the surface distribution of the energy flux of such stars as well as their precise shape on the background sky. Data are usually fit by a simple brightness law derived from a Roche-von Zeipel model (e.g. Domiciano de Souza et al., 2002) where it is assumed that the shape of the star is determined by a Roche model (all the mass is concentrated in the center) while the brightness distribution obeys von Zeipel law, namely the energy flux being proportional to local effective gravity. If such a model is efficient at giving a first interpretation of the observation and especially getting an idea of the orientation of the stellar rotation axis as well as its angular velocity, one now wishes to go beyond this simple model. This step is however difficult as it means building a self-consistent two-dimensional model of a star and then being able to make it evolve till the assumed age of the observed object.

Many attempts have been done to reach this goal but most of them did not go beyond the construction of barotropic stars without any dynamics or evolution (see the recent work of Roxburgh, 2004, Jackson et al., 2005). The inclusion of fluid dynamics is however important for the models to be physically self-consistent. Rotating stars are indeed baroclinic and fluid flows are present everywhere, even in radiative zones. Their long term effect is the mixing of elements and the transport of angular mo-

mentum (see Zahn, 1992). They cannot be ignored in the evolution of rotating stars.

Previous work on models of baroclinic stars is scarce: only Uryu & Eriguchi (1994, 1995) constructed global 2D models of rapidly rotating stars with baroclinicity, but their neglect of viscosity removed any meridional circulation and left differential rotation undetermined. More recently, Rieutord (2006) used a Boussinesq model (*i.e.* a nearly incompressible fluid) for investigating the baroclinic flows at global scale. In this case, it could be shown how viscosity determines the differential rotation and that this latter strongly depends on the Prandtl number.

The present work aims at describing a more realistic approach, physically self-consistent, of a rotating fully radiative star. Of course this is a model and real physics is still much simplified but no arbitrary assumption needs to be made. In a few words our model can be described as follows: we consider a perfect gas contained in a rigid sphere; the gas is rotating and self-gravitating; the mass inside the sphere is large enough so that the central temperature and density permit nuclear reactions. The gas is a viscous fluid conducting heat through radiative diffusivity derived from Kramers type opacities. The bounding sphere allows us to impose simple (but physically relevant) boundary conditions on the gravitational potential, temperature, pressure and velocity field. Roughly speaking, these conditions specify that the gravitational potential connect to the one pervading vacuum, that temperature connects to the temperature field of a medium with a constant absorption coefficient radiating like a black body, that some radial stress can be accepted by the bounding sphere but that matter slips freely and tangentially on the sphere. This set-up, which is similar to a laboratory experiment, simplifies the numerical resolution of the equations by allowing the use of spherical coordinates while the distribu-

tion of mass is not spherically symmetric. Fortunately, the bulk properties of this “star” do not depend very much on the physics imposed at the outer boundary. The next step will be to replace the sphere by a spheroid which perfectly fits an isobar; however, this step, which needs using spheroidal coordinates with multi-domains, is numerically challenging and can be undertaken only on a physically understood system.

We have voluntarily removed the convection zones which need a generalization of the mixing-length theory in two-dimensions including the effects of rotation. Here we focus on a rotating radiative star and examine the dynamical properties of its baroclinic state.

The paper is organised as follows: We next describe our model (Sect. 2) and the numerical methods we use for solving the equations (Sect. 3). We then describe some tests of the model showing internal accuracy and how they compare to one-dimensional models (Sect. 4). In Sect. 5 results are presented and conclusions follow.

2. The model

2.1. Description

We consider a viscous, self-gravitating fluid rotating with a mean angular velocity $\mathbf{\Omega} = \Omega \mathbf{e}_z$. The fluid is supposed to be inside an undeformable sphere of radius R , so the outer boundary can be taken at $r = R$; this simplifies the problem by allowing the use of spherical coordinates to represent the variables, although the external boundary does not fit an isobar.

In a steady configuration, the fluid is governed by the following equations:

$$\begin{cases} \Delta\phi = 4\pi G\rho \\ \rho T \mathbf{v} \cdot \nabla s = -\nabla \cdot \mathbf{F} + \varepsilon \\ \rho (2\mathbf{\Omega} \times \mathbf{v} + \mathbf{v} \cdot \nabla \mathbf{v}) = -\nabla P - \rho \nabla \left(\phi - \frac{1}{2} \Omega^2 r^2 \sin^2 \theta \right) + \mathbf{F}_v \\ \nabla \cdot (\rho \mathbf{v}) = 0 \end{cases} \quad (1)$$

where ϕ is the gravitational potential, ρ the density, s the specific entropy, T the temperature, \mathbf{v} the fluid velocity with respect to a frame rotating at angular velocity $\mathbf{\Omega}$. P is the pressure and ε the nuclear energy generation rate per unit volume. For a compressible fluid with constant dynamical viscosity μ , the viscous force can be written as

$$\mathbf{F}_v = \mu \left(\Delta \mathbf{v} + \frac{1}{3} \nabla (\nabla \cdot \mathbf{v}) \right) \quad (2)$$

For the energy flux, we will consider only radiative transport,

$$\mathbf{F} = -\chi \nabla T \quad (3)$$

where $\chi(\rho, T)$ is the radiative diffusivity. The equation of state is that of an ideal gas mixed with photons; hence we use

$$p = \mathcal{R}_M \rho T + \frac{a}{3} T^4 \quad (4)$$

where \mathcal{R}_M is the gas constant divided by the mean molecular weight and a the radiation density constant.

2.2. Stellar microphysics

We assume that the fluid is in the conditions of a stellar plasma typical of the sun’s radiative zone. Nuclear energy generation rate per unit volume is of the form

$$\varepsilon = \varepsilon_0 X^2 \rho^2 T^{-2/3} e^{-bT^{-1/3}} \quad (5)$$

where X is the hydrogen mass fraction; for the constants ε_0 and b we adopt the values of the CESAM code (Morel, 1997), namely $b = 3600$ and $\varepsilon_0 = 8.37 \cdot 10^{10}$ (cgs) (6)

for the pp-chain.

In order to describe the radiative transport of energy, we use the opacity given by a Kramer’s law type

$$\kappa = \kappa_0 T^{-\beta} \rho^\eta \quad (7)$$

so that the radiative diffusivity can be written as

$$\chi = \frac{16\sigma T^3}{3\kappa\rho} = \chi_0 T^{\beta+3} \rho^{-\eta-1} \quad (8)$$

In particular we use $\beta = 1.97541$, $\eta = 0.138316$ and $\kappa_0 = 7.1548412 \cdot 10^{13}$ cgs, following some fitting formulae¹ proposed by J. Christensen-Dalsgaard for simple solar models (e.g. Christensen-Dalsgaard & Reiter, 1995).

2.3. Boundary conditions

In order to solve the full system of equations we must complete it with boundary conditions. At the center of the star ($r = 0$) we just need to impose regularity of the solutions. At the outer boundary, *i.e.* on the rigid bounding sphere, we shall impose that the fluid slips freely and thus use stress-free boundary conditions. Hence, we have

$$u_r = \sigma_{r\theta} = \sigma_{r\varphi} = 0 \quad \text{at } r = R \quad (9)$$

where $\sigma_{r\theta}$ and $\sigma_{r\varphi}$ are the horizontal components of the stress on the outer sphere.

Since the sphere is rigid, it can support some normal stress and pressure is not constant on it as well as the density and temperature. As the true surface of the star is outside the box, pressure needs to be fixed somewhere. We shall thus impose the polar pressure. This condition imposes the place where our container “cuts” the star envelope.

About temperature, usual boundary conditions are that the boundary radiates like a black body; we thus write

$$-\chi \frac{\partial T}{\partial r} = \sigma T^4 \quad \text{at } r = R$$

Using the expression of radiative diffusivity, this condition is equivalent to

$$\frac{\partial T}{\partial r} + \sigma_T T = 0$$

where $\sigma_T = 3\rho\kappa/16$. Obviously, σ_T depends on latitude but in order to avoid unnecessary complications (nonlinearities) we take it as a constant. Physically, this means that at the boundary the fluid meets a medium with constant absorption coefficient radiating like a black body.

Finally, the boundary conditions on the gravitational potential are the matching with the vacuum solution which vanishes at infinity.

¹ The proposed formula is $\frac{1}{\kappa} = \frac{1}{\kappa_i} + \frac{1}{\kappa_e}$ with κ_i as in (7) and $\kappa_e = 1.6236784 \cdot 10^{-33} \rho^{0.407895} T^{9.28289}$; we use only the “interior” opacity, leaving the “envelope” one.

2.4. Dimensionless equations

We scale the physical quantities, so that the solutions are of order unity. For that, we choose the free-fall time scale $\lambda = (4\pi G \rho_c)^{-1/2}$, the radius of the container R as the length scale, the central values of temperature T_c and density ρ_c for the corresponding scales and the gas constant \mathcal{R}_M for the entropy scale. With dimensionless variables the equations are now written as

$$\begin{cases} \Delta\phi = \rho \\ \frac{\mathcal{P}}{E} \rho T \mathbf{u} \cdot \nabla s = \nabla \cdot (\chi \nabla T) + \Lambda \varepsilon \\ \rho (2\Omega \times \mathbf{u} + \mathbf{u} \cdot \nabla \mathbf{u}) = -\nabla p - \rho \nabla \phi_{\text{eff}} + E \mathbf{F}_u \\ \nabla \cdot (\rho \mathbf{u}) = 0 \\ p = \pi_c \left(\rho T + \frac{1-\beta_c}{\beta_c} T^4 \right) \end{cases} \quad (10)$$

where $\phi_{\text{eff}} = \phi - \frac{1}{2} \Omega^2 r^2 \sin^2 \theta$ and $\mathbf{F}_u = \Delta \mathbf{u} + \frac{1}{3} \nabla (\nabla \cdot \mathbf{u})$; we also introduced the dimensionless numbers

$$E = \frac{\mu \lambda}{\rho_c R^2}, \quad \mathcal{P} = \frac{\mu \mathcal{R}_M}{\chi_c}.$$

E is a kind of Ekman number associated with the limit angular velocity $\sqrt{4\pi G \rho_c}$ and \mathcal{P} is the Prandtl number at the center. The Ekman number measures the importance of viscous force relative to Coriolis force and its true definition is E/Ω ; here we had to keep out the non-dimensional rotation rate for convenience. In stellar conditions $E/\Omega \ll 1$. Other, more stellar, dimensionless numbers have been introduced:

$$\pi_c = \frac{\mathcal{R}_M T_c \lambda^2}{R^2}, \quad \Lambda = \frac{\varepsilon_c R^2}{\chi_c T_c} \quad \text{and} \quad \beta_c = \frac{\pi_c}{\pi_c + \frac{a T_c^4 \lambda^2}{3 \rho_c R^2}}$$

π_c is the dimensionless central gas pressure and β_c the usual ratio of gas to total pressure at the star center. Once we fix the microphysics of the problem, the dimensionless numbers π_c and Λ should appear as part of the solution as they determine the central temperature and density (or mass) of the configuration.

The quantities χ and ε have been scaled using their central values χ_c and ε_c , so that the dimensionless radiative diffusivity and energy generation rate are given by

$$\chi = T^{\beta+3} \rho^{-\eta-1} \quad \text{and} \quad \varepsilon = \rho^2 T^{-2/3} e^{-\alpha(T^{-1/3}-1)} \quad (11)$$

where $\alpha = b T_c^{-1/3}$. Using these expressions and writing the entropy gradient as a function of the temperature and pressure gradients, the equation of energy balance reads

$$\Delta T + \nabla \ln \chi \cdot \nabla T - \frac{\mathcal{P}}{E} \mathbf{a} \cdot \mathbf{u} = -\Lambda \frac{\rho^{\eta+3}}{T^{\beta+11/3}} e^{-\alpha(T^{-1/3}-1)} \quad (12)$$

where we introduced the vector:

$$\mathbf{a} = \frac{\rho^{\eta+1}}{T^{\beta+3}} \left(\frac{\gamma}{\gamma-1} \rho \nabla T - \frac{1}{\pi_c} \nabla p \right) \quad (13)$$

which explicits the entropy gradient; γ is the adiabatic exponent.

The scaling of the velocity field requires some consideration. In Rieutord (2006) it is shown that the meridional circulation, *i.e.* the radial and meridional components of the velocity field, is proportional to the Ekman number, therefore we write:

$$\mathbf{u} = Eu_r \mathbf{e}_r + Eu_\theta \mathbf{e}_\theta + u_\varphi \mathbf{e}_\varphi \quad (14)$$

The system (10) is the set of nonlinear PDE which governs the radiative zone of a rotating star when no turbulence or magnetic field troubles the place. It is this system which will give us the first view of the dynamics inside the central parts of a rapidly rotating fully radiative star.

3. Numerical Method

3.1. Why spectral methods

One dimensional stellar evolution codes usually use a few thousand of grid points to model and follow the evolution of a star. With the same kind of discretization (*i.e.* finite differences), the number of grid points would grow by a factor of a few hundred for a two-dimensional model. Such a number of points is certainly very heavy to manage; two dimensional models require more efficient discretization and this is why we adopted spectral methods.

Spectral methods are best-known for their precision when the number of grid points is limited (Peyret, 2002, Grandclément, 2006, Bonazzola et al., 1999). On the dark side, they have never been used in stellar modelling (to our knowledge) and are rather “touchy” as far as stability is concerned; more particularly, discontinuities require special care like a multi-domain approach. Nevertheless, the precision they can reach is a major advantage, especially when the oscillation spectrum of a star needs to be computed. The advances in observational asteroseismology, with space missions like COROT, require indeed very precise models (Reese et al., 2006).

The discretization of the equations is made via an expansion of the unknowns onto the spherical harmonic basis for the angular part and using Gauss-Lobatto collocation nodes for the radial part. This latter grid is associated with Chebyshev polynomials (*e.g.* Canuto et al., 2006, Fornberg, 1998).

3.2. Projection on the spherical harmonics

The variables are thus first projected on the spherical harmonics. Hence, for the scalar quantities:

$$f = \sum_l f_l(r) Y_l^0(\theta) \quad (15)$$

Note that, due to the symmetry of the problem, solutions are axisymmetric and therefore $m = 0$. For the velocity, we follow Rieutord (1987) and use the expansion:

$$\mathbf{u} = \sum_l Eu_l(r) \mathbf{R}_l^0 + Ev_l(r) \mathbf{S}_l^0 + w_l(r) \mathbf{T}_l^0 \quad (16)$$

where the vectorial spherical harmonics are

$$\begin{aligned} \mathbf{R}_l^m &= Y_l^m \mathbf{e}_r \\ \mathbf{S}_l^m &= \frac{\partial Y_l^m}{\partial \theta} \mathbf{e}_\theta + \frac{1}{\sin \theta} \frac{\partial Y_l^m}{\partial \varphi} \mathbf{e}_\varphi \\ \mathbf{T}_l^m &= \frac{1}{\sin \theta} \frac{\partial Y_l^m}{\partial \varphi} \mathbf{e}_\theta - \frac{\partial Y_l^m}{\partial \theta} \mathbf{e}_\varphi \end{aligned} \quad (17)$$

The projection of the momentum equation yields three equations:

$$\begin{aligned} \frac{dp_l}{dr} + 2 \langle \rho \rangle \Omega [(l-1) \alpha_l w_{l-1} - (l+2) \alpha_{l+1} w_{l+1}] \\ - E^2 \left[\frac{4}{3} \frac{d^2 u_l}{dr^2} + \frac{8}{3r} \frac{du_l}{dr} - \frac{(l(l+1) + 8/3)}{r^2} u_l \right. \\ \left. - \frac{l(l+1)}{3r} \frac{dv_l}{dr} + \frac{7l(l+1)}{3r^2} v_l \right] = \text{rhsu}_l \end{aligned}$$

$$\begin{aligned} \frac{p_l}{r} + 2 \langle \rho \rangle \Omega \left[\frac{l-1}{l} \alpha_l w_{l-1} + \frac{l+2}{l+1} \alpha_{l+1} w_{l+1} \right] \\ - E^2 \left[\frac{d^2 v_l}{dr^2} + \frac{2}{r} \frac{dv_l}{dr} - \frac{4l(l+1)}{3r^2} v_l + \frac{1}{3r} \frac{du_l}{dr} + \frac{8}{3r^2} u_l \right] = \text{rhsv}_l \end{aligned}$$

$$2 \langle \rho \rangle \Omega \left[\frac{\alpha_l}{l} u_{l-1} - \frac{\alpha_{l+1}}{l+1} u_{l+1} - \frac{l-1}{l} \alpha_l v_{l-1} - \frac{l+2}{l+1} \alpha_{l+1} v_{l+1} \right] - \left[\frac{d^2 w_l}{dr^2} + \frac{2}{r} \frac{dw_l}{dr} - \frac{l(l+1)}{r^2} w_l \right] = \text{rhs} w_l$$

where we have introduced the spherically averaged quantities

$$\langle f \rangle = \frac{1}{4\pi} \int_{4\pi} f d\Omega = \frac{f_0(r)}{\sqrt{4\pi}} \quad (18)$$

and the coupling coefficient

$$\alpha_l = \frac{l}{\sqrt{4l^2 - 1}} \quad (19)$$

The other equations yield:

$$\frac{d^2 \phi_l}{dr^2} + \frac{2}{r} \frac{d\phi_l}{dr} - \frac{l(l+1)}{r^2} \phi_l = \rho_l \quad (20)$$

$$\frac{du_l}{dr} + \frac{2u_l}{r} - \frac{l(l+1)}{r^2} v_l = \text{rhs} d_l \quad (21)$$

$$\frac{dT_l}{dr^2} + \left(\frac{2}{r} + \frac{d}{dr} \langle \ln \chi \rangle \right) \frac{dT_l}{dr} - \frac{l(l+1)}{r^2} T_l - \mathcal{P} \langle a_r \rangle u_l = \text{rhs} t_l \quad (22)$$

The right-hand side terms are essentially non-linear terms which are gathered in Table 1.

3.3. Boundary conditions

Boundary conditions have to be expressed on the radial functions.

Regularity of the solutions at the star center demands the regularity of the radial functions at $r = 0$; as far as the pressure is concerned, we fix the polar value to p_s which fixes the constant needed by the solution of the momentum equation. Stress-free boundary conditions on the velocity field give (Rieutord, 1987),

$$\begin{cases} u_l = 0 \\ r \frac{dv_l}{dr} - v_l = 0 \\ r \frac{dw_l}{dr} - w_l = 0 \end{cases} \quad \text{at the surface} \quad (26)$$

The gravitational potential at the surface matches that of the vacuum

$$r \frac{d\phi_l}{dr} + (l+1)\phi_l = 0 \quad \text{at } r = 1 \quad (27)$$

Finally, the radial functions of the temperature verify

$$r \frac{dT_l}{dr} + \sigma_T T_l = 0 \quad \text{at the surface} \quad (28)$$

3.4. Algorithm for iterations

Equations are solved iteratively because of nonlinearities; we follow and generalize the algorithm used by Bonazzola et al. (1998) for polytropic stellar models. The idea is to set the equations in the form

$$\mathcal{L}_n(\mathbf{y}_{n+1}) = \text{RHS}(\mathbf{y}_n, \mathbf{y}_{n-1})$$

where \mathcal{L}_n is a linear operator which may depend on the n -th iterate. Such a scheme is also known as the fixed point algorithm. Convergence depends on the norm of the linear operator and the closeness to the solution; the dependence of RHS with respect to \mathbf{y}_{n-1} stands for the relaxation terms. Unlike Henyey's method which is a Newton type algorithm, this scheme does not need the computation of the jacobian matrix which is quite unpractical with our discretization and high order operators.

4. Tests of the model

4.1. Internal accuracy

In Fig. 1 we show the spectra of the different physical quantities; as these spectra are scaled by the maximum value, they show the internal relative precision of the solutions due to truncation. On this example spectral convergence is very good on the gravitational potential, pressure, temperature and less good on the velocity components; this latter quantity is indeed facing rapid variations in the boundary (Ekman) layers.

Although spectra give a good idea of the precision of the solution, they do not tell the whole story. Indeed, round-off errors are also affecting the solution as they are usually amplified by the resolution of linear systems (backward error) and may have a devastating effect (e.g. Valdetaro et al., 2006). In our case, round-off errors have been tested on "eigenvalues" like π_c and Λ and were found below $5 \cdot 10^{-8}$.

4.2. The virial equality

A standard test to assess the accuracy of the computations of a rotating, self-gravitating fluid, is the virial equality (see Ostriker & Bodenheimer, 1968, Eriguchi & Müller, 1985). This is indeed an integral form of the momentum equation along with mass conservation. Since this equality has only been used with barotropic stars, we give here its full expression appropriate for a baroclinic star.

We first rewrite the momentum and continuity equations as

$$(2\boldsymbol{\Omega} \wedge \rho \mathbf{u})_i + \rho u_j \partial_j u_i = -\rho \partial_i \phi + \rho \Omega^2 s(\mathbf{e}_s)_i + \partial_j \sigma_{ij} \quad (29)$$

$$\partial_j \rho u_j = 0 \quad (30)$$

where σ_{ij} stands for the stress tensor (including the pressure), namely:

$$\sigma_{ij} = -P \delta_{ij} + \mu \left(\partial_i v_j + \partial_j v_i - \frac{2}{3} (\partial_k v_k) \delta_{ij} \right)$$

On the outer boundary, we imposed stress-free boundary conditions, i.e. $u_r = \sigma_{r\theta} = \sigma_{r\varphi} = 0$. The volume integral of the scalar product of (29) with \mathbf{r} yields the virial identity

$$2T_{\text{rel}} + I\Omega^2 + W + 3P + I_s + 2\Omega L_z = 0$$

where we introduced:

$$T_{\text{rel}} = \frac{1}{2} \int_{(V)} \rho u^2 dV$$

the kinetic energy in the rotating frame,

$$I = \int_{(V)} \rho r^2 \sin^2 \theta dV$$

$$\begin{aligned}
\mathbf{RHS}_{\text{mom}} &= \sum (\text{rhsu}_l \mathbf{R}_l^0 + \text{rhsv}_l \mathbf{S}_l^0 + \text{rhw}_l \mathbf{T}_l^0) \\
&= \left[-\rho \frac{\partial}{\partial r} \left(\phi - \frac{1}{2} \Omega^2 r^2 \sin^2 \theta \right) + 2\delta\rho\Omega u_\varphi \sin \theta + \frac{\rho u_\varphi^2}{r} + E^2 \rho \left(\frac{u_\theta^2}{r} - u_r \frac{\partial u_r}{\partial r} - \frac{u_\theta}{r} \frac{\partial u_r}{\partial \theta} \right) \right] \mathbf{e}_r + \\
&\quad \left[-\frac{\rho}{r} \frac{\partial}{\partial \theta} \left(\phi - \frac{1}{2} \Omega^2 r^2 \sin^2 \theta \right) + 2\delta\rho\Omega u_\varphi \cos \theta + \frac{\rho u_\varphi^2}{r} \cot \theta - E^2 \rho \left(\frac{u_\theta u_r}{r} + u_r \frac{\partial u_\theta}{\partial r} + \frac{u_\theta}{r} \frac{\partial u_\theta}{\partial \theta} \right) \right] \mathbf{e}_\theta + \\
&\quad \left[-2\delta\rho\Omega (u_r \sin \theta + u_\theta \cos \theta) - \rho \left(\frac{u_\varphi}{r} (u_r + u_\theta \cot \theta) + u_r \frac{\partial u_\varphi}{\partial r} + \frac{u_\theta}{r} \frac{\partial u_\varphi}{\partial \theta} \right) \right] \mathbf{e}_\varphi
\end{aligned} \tag{23}$$

$$\text{rhsd} = -\mathbf{u} \cdot \nabla \ln \rho \tag{24}$$

$$\text{rhst} = -\Lambda \frac{\rho^{\eta+3}}{T^{\beta+11/3}} e^{-\alpha(T^{-1/3}-1)} + \frac{\mathcal{P}}{E} \delta \mathbf{a} \cdot \mathbf{u} - \nabla \delta \ln \chi \cdot \nabla T \tag{25}$$

Table 1. In these expressions δ denotes the non-spherical part of a variable $\delta f = f - \langle f \rangle$.

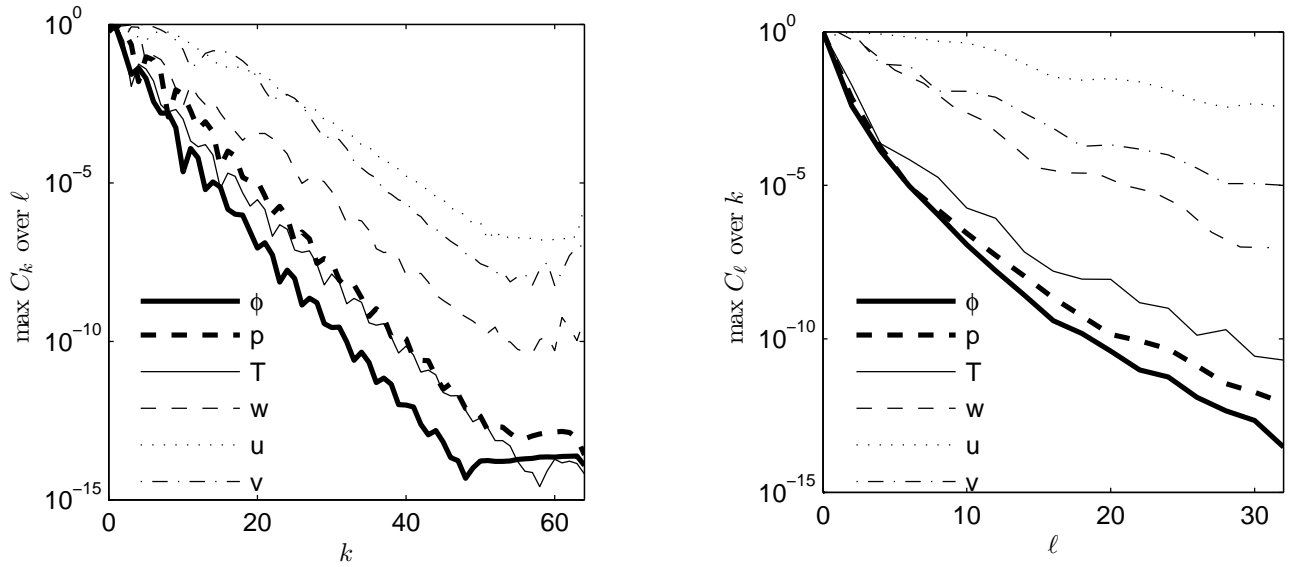


Fig. 1. Spectral convergence of the various physical quantities of the model. On left: scaled coefficient of the Chebyshev polynomial expansion (maximized over the spherical harmonic degrees); on right: the corresponding spectral coefficients of the spherical harmonics maximized over the Chebyshev coefficients. These curves have been obtained with a model where $p_s = 10^{-5}$, $E = 10^{-8}$, $\Omega = 0.07$, $\alpha = 15.2$, $\sigma_T = 1.5$.

the momentum of inertia,

$$W = \frac{1}{2} \int_{(V)} \rho \phi d^3 \mathbf{r}$$

the gravitational potential energy,

$$3P = - \int_{(V)} \sigma_{ii} dV$$

the internal energy,

$$I_s = \int_{(S)} r_i \sigma_{ij} dS_j$$

the surface stress and

$$L_z = \mathbf{e}_z \cdot \int_{(V)} \mathbf{r} \wedge \rho \mathbf{u} dV$$

the relative angular momentum z-component. The last two integrals may be vanishingly small if the background rotation contains all the angular momentum and if the boundary of the domain is near the zero pressure surface.

Ω	Virial
10^{-8}	$-5.4 \cdot 10^{-8}$
0.05	$-1.4 \cdot 10^{-8}$
0.1	$-1.3 \cdot 10^{-8}$
0.15	$1.4 \cdot 10^{-7}$

Table 2. Values of the virial equality scaled by the gravitational energy for different rotation velocities. We have used 32 radial points, $l_{\text{max}} = 16$, Ekman number $E = 10^{-5}$ and surface pressure $p_s = 10^{-3}$. For comparison, the break-up velocity for these models is $\Omega_k \sim 0.2$.

We give in Table 2 the value of the virial equality scaled, as usual by the gravitational energy W . We find values less than 10^{-7} thanks to spectral precision as in Bonazzola et al. (1998); these values can be compared with 10^{-3} obtained by Uryu & Eriguchi (1994, 1995) or $10^{-4} - 10^{-5}$ by Jackson et al. (2005) resulting from the finite difference discretizations.

	ESTER	CESAM
Mass	3.05	3.00
Radius	2.40	2.29
Luminosity	107.	107.
ρ_c	129	132
π_c	$1.39 \cdot 10^{-3}$	$1.48 \cdot 10^{-3}$
Λ	232	219

Table 3. Comparison of the results between the two-dimensional code ESTER run at zero rotation and the one-dimensional code CESAM. The central temperature is fixed to $3.05 \cdot 10^7$ and hydrogen mass fraction is $X=0.712$.

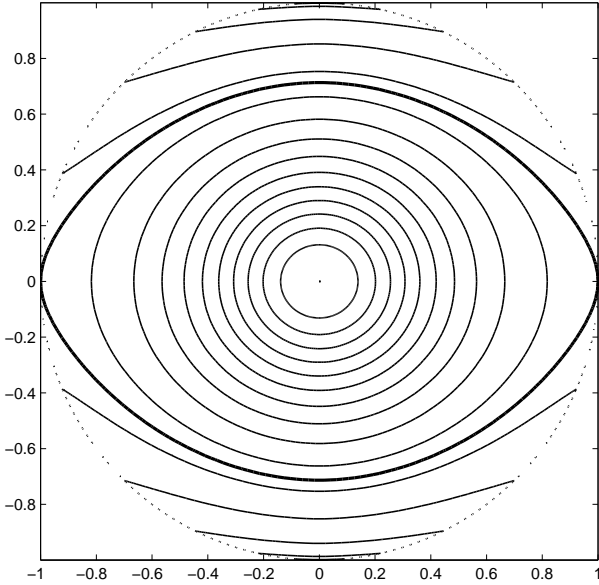


Fig. 2. Isobars for a model with $\Omega = 0.07$. An equatorial keplerian velocity for this case is reached when $\Omega_k = 0.082$, so the star is rotating at 85% of its break-up velocity. Other parameters are standard (see text). The thick isobar underlines the last complete isobar allowed by the container.

4.3. Calibration with one-dimensional models

In the dimensionless formulation the two numbers Λ and π_c are of special importance. They give the radius, the central temperature and the central density once the mass is fixed. π_c is indeed a non-dimensional measure of the central pressure while Λ of central heating. Using the expression of these numbers we note that their product

$$\Lambda \pi_c = \frac{\mathcal{R} \varepsilon_c}{4\pi G \rho_c \chi_c}$$

depends only on central density and central temperature; thus, its determination yields a first relation between these two quantities. The expression of the mass

$$M = \rho_c R^3 \int_{(V)} \rho dV$$

combined with that of Λ gives another relation between T_c and ρ_c and therefore allows for the determination of R, T_c, ρ_c . Actually, for convenience we prefer fixing the central temperature instead of the mass and derive the other quantities.

As a first test of the model we compare the results obtained for a non-rotating configuration with the results of a one-

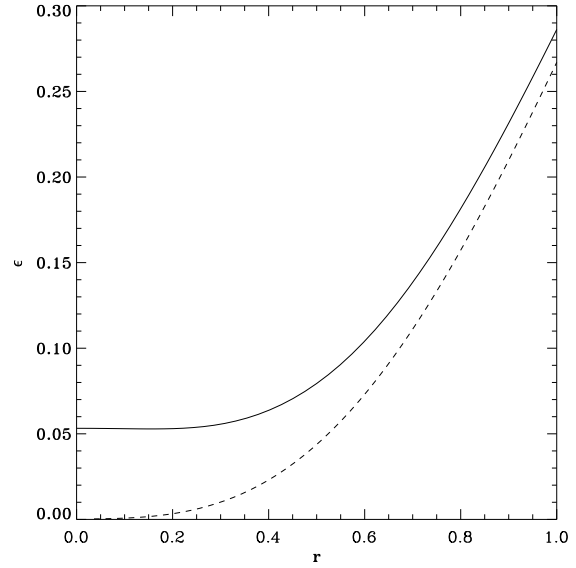


Fig. 3. Flatness $\epsilon = 1 - \frac{R_{\text{pol}}}{R_{\text{eq}}}$ of the isobars as a function of the equatorial radius for our model (solid line) and for the polytrope of index 4.37 rotating at 82% of the critical velocity. $p_s = 10^{-5}$, $E = 10^{-8}$, $\Omega = 0.07$, $\alpha = 15.2$, $\sigma_T = 1.5$.

dimensional code like CESAM (Morel, 1997). We show the results in Table 3. The physics of the one-dimensional code was made as close to ours as possible but surface boundary conditions, implying some superficial convection, still make noticeable differences (the three solar mass was chosen to minimize the effects of convection although the physics does not strictly apply in this case). Nevertheless, the results displayed in this table show that our model is close to models computed with traditional stellar evolution codes. Thus, we have in our “box” a self-gravitating fluid close to the stellar conditions.

We do not ask for more precision at the moment since all the physics is not implemented; we leave for future work a more detailed comparison. Presently, we estimate that mass and temperature distributions are sufficiently close to “reality” that our fluid flows are meaningful (as long as turbulence is negligible).

5. Results

For all the examples shown below, we use a polar pressure of $p_s = 10^{-5}$ (scaled by central pressure), a rotation rate of $\Omega = 0.07$ which is about 82% of the critical angular velocity, a central temperature of $T_c = (b/\alpha = 15.2)^3 = 1.33 \cdot 10^7$ K, $\sigma_T = 1.5$ and $\beta_c = 1$ (we neglect radiation pressure); Ekman number is set to 10^{-8} and Prandtl number to zero. The mass enclosed in the container is close to one solar mass.

Table 4 summarizes the properties of the models when rotation is increased. We note that the mass slightly increases as well as the luminosity while the radius and the central density slightly decrease. This is a consequence of our choice of keeping constant the central temperature and the ratio of polar pressure to central pressure.

5.1. Internal structure

The first view of the internal structure is given by the pressure distribution as shown in Fig. 2. We emphasize the “last isobar”

Ω	0.01	0.02	0.03	0.04	0.05	0.06	0.07
Mass (M_\odot)	1.003	1.009	1.018	1.032	1.050	1.074	1.105
Radius (R_\odot)	0.9955	0.9941	0.9918	0.9883	0.9833	0.9765	0.9674
Luminosity (L_\odot)	0.803	0.805	0.808	0.811	0.816	0.822	0.829
ρ_c (g/cm ³)	86.5	86.4	86.3	86.2	86.0	85.8	85.6
π_c	$5.16 \cdot 10^{-3}$	$5.18 \cdot 10^{-3}$	$5.21 \cdot 10^{-3}$	$5.268 \cdot 10^{-3}$	$5.32 \cdot 10^{-3}$	$5.41 \cdot 10^{-3}$	$5.53 \cdot 10^{-3}$
Λ	69.2	69.4	69.0	68.7	66.9	65.5	63.7

Table 4. Parameters of our purely radiative star for various rotation rates; numerics use a radial grid with $N_r=64$ points and the maximum degree of spherical harmonics is $L_{\max}=32$. We use $p_s = 10^{-5}$, $T_c = 1.3285 \cdot 10^7$ K, $\sigma_T = 1.5$ and $\beta_c = 1$; hydrogen mass fraction is $X=0.71$ and $Z=0$. Ekman number is $E = 10^{-8}$.

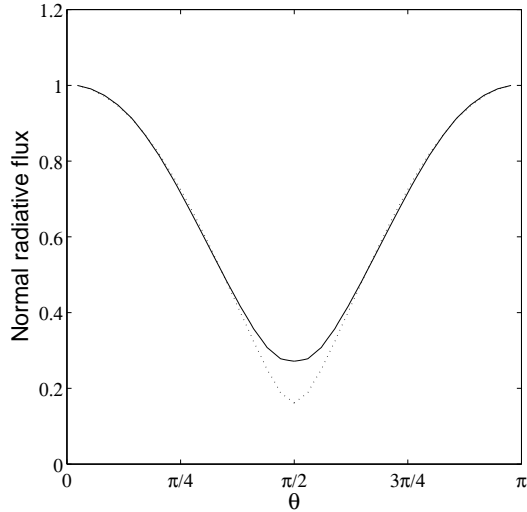


Fig. 4. Normal radiative flux at the last isobar ($p = p_{\text{eq}}$), real values (solid line) and von Zeipel model (dotted line). von Zeipel model is calculated from the normal effective gravity; both curves have been scaled by their polar value.

with a thick line; this is the last complete isobar fitting in the container; we shall use it below to appreciate the latitude variations of the flux and temperature.

Mass distribution can be appreciated by the flatness profile of the isobars as shown in Fig. 3. It is well known that a stellar envelope with Kramers' type opacities behaves like a polytropic envelope of index $n = (\beta + 3)/(\eta + 1)$ which is ~ 4.37 in our case. Thus, for comparison, we also show the flatness of the isobar of a fully polytropic star rotating at 85% of the breakup velocity. The curves show that the polytrope is much more centrally condensed than the star as the flatness of isobars are almost zero at the center.

We then computed the energy flux surface density at the last isobar contained in the domain (the thick line in Fig. 2) and compared it to the one given by the von Zeipel model. We recall that von Zeipel model assumes that the star is barotropic and thus density and temperature depend only on the effective potential (*i.e.* gravitational plus centrifugal); it follows that the energy flux is proportional to the local effective gravity. Fig. 4 shows that the von Zeipel model overestimates the contrast of the polar and equatorial flux. Actually, the ratio of polar to equatorial flux is 3.68 for our model while it is 6.2 for von Zeipel one, almost two times larger.

As far as temperature is concerned, we computed the variation of temperature along the last isobar. As shown in Fig. 5, the temperature drops noticeably at the equator, *i.e.* by a few 10^5 K.

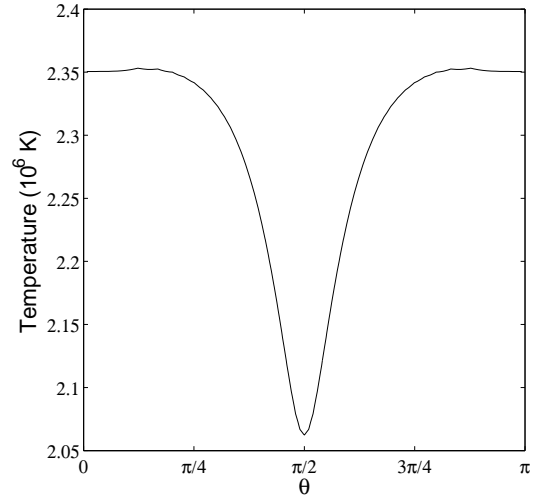


Fig. 5. Variations of temperature along the last isobar.

The temperature drop shows that isothermal surfaces are more spherical than the isobars.

Next we considered the local Brunt-Väisälä frequency which, as shown in Rieutord (2006), controls the baroclinic torque. This quantity is plotted in Fig. 6 for a rotation of $\Omega = 0.03$ and in Fig. 7 for the usual rotation $\Omega = 0.07$. Quite interestingly, we see that if rotation is fast enough, the local Brunt-Väisälä frequency is imaginary in the equatorial region revealing the appearance of a convection zone driven by the cool equator. Of course in such a region the model that we have used is no longer valid as one should take into account the entropy mixing of turbulent convection. However, we think that we show here, for the first time, the emergence of an equatorial convection zone due a fast rotation. In Fig. 8 we underline the anisotropy of the squared Brunt-Väisälä frequency distribution by comparing the poleward and equatorward profiles. This anisotropy will impact on the low-frequency spectrum of oscillations (gravito-inertial modes) as can be surmised from Dintrans & Rieutord (2000).

5.2. Differential rotation and circulation

We now turn to the dynamical state of our radiative “star”. Since we simplified the solutions by focusing only on the axisymmetric steady ones, the dynamics of the star is described by its differential rotation and meridional circulation. We give in Fig. 9 the typical shape of isorotation lines in a meridian plane. These do not change much with rotation. The main property of this baroclinic flow is that the equator rotates faster than the pole.

This shape of the differential rotation can be understood from the torque balance in the momentum equation. Indeed, neglecting nonlinear and viscous terms, the curl of the momentum equa-

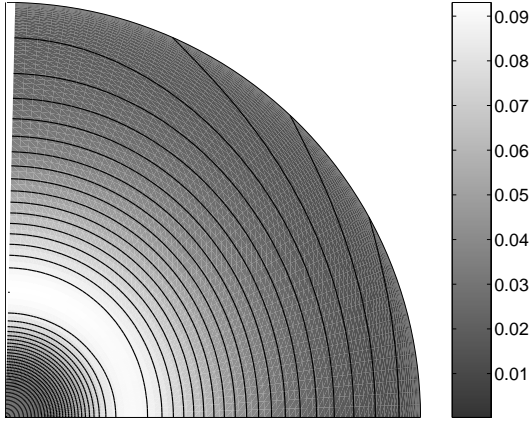


Fig. 6. Square of the Brunt-Väisälä frequency N^2 when the rotation is $\Omega = 0.03$.

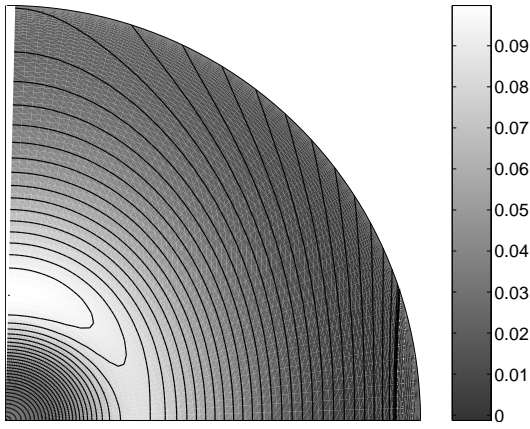


Fig. 7. Same as in Fig. 6 but with $\Omega = 0.07$. Dotted lines are for negative contours, in which there is convective instability. The thick line represents the points where $N^2 = 0$.

tion in (10) together with the equation of state, yield the baroclinic balance, namely,

$$\frac{\partial u_\varphi}{\partial z} = \pi_c (\nabla T \times \nabla \ln P)_\varphi$$

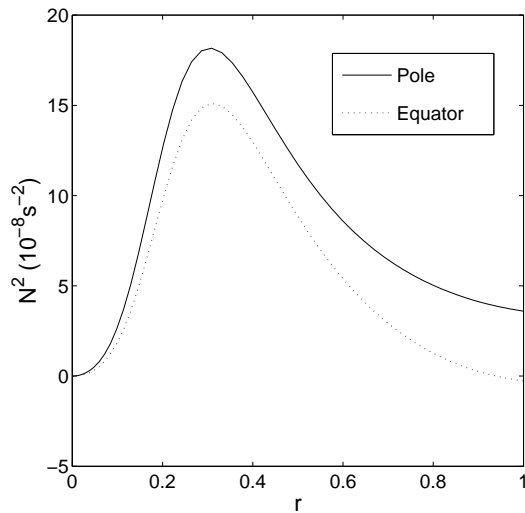


Fig. 8. Brunt-Väisälä frequency profile at pole and equator when $\Omega = 0.07$.

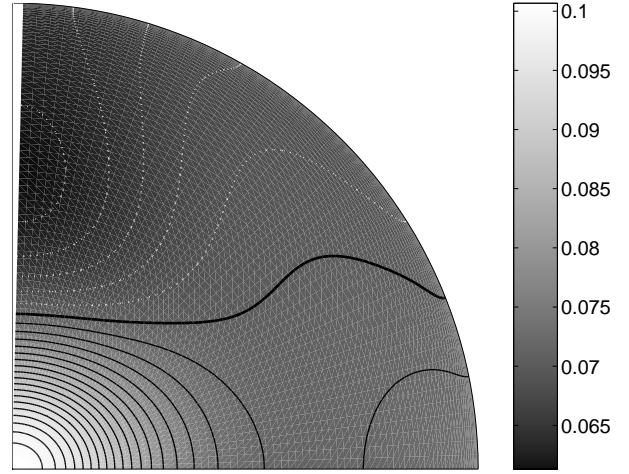


Fig. 9. Differential rotation, the thick line corresponds to $\Omega = 0.07$ which is the background rotation rate; faster and slower rotation are represented by solid black lines and dotted white lines respectively.

Now, if we consider the latitudinal variation of the temperature along an isobar, replacing the radial variable by the pressure, we may write $T \equiv T(P, \theta)$ and thus

$$\nabla T = \frac{\partial T}{\partial P} \nabla P + \left(\frac{\partial T}{\partial \theta} \right)_P \nabla \theta$$

We can therefore rewrite the baroclinic balance as

$$\frac{\partial u_\varphi}{\partial z} = -\frac{\pi_c}{r} \left(\frac{\partial T}{\partial \theta} \right)_P \frac{\partial \ln P}{\partial r} \quad (31)$$

Since in any direction, pressure decreases with r and isotherms are more spherical than isobars (temperature decreases on an isobar from pole to equator), we find that $\frac{\partial u_\varphi}{\partial z} < 0$. The baroclinic torque thus makes the polar region rotating slower than the equatorial regions.

This result is (unfortunately!) at odds with the solution of the Boussinesq model devised in Rieutord (2006) where the polar rotation turned out to be faster than the equatorial one. In the Boussinesq model, the baroclinic balance leads to

$$\frac{\partial u_\varphi}{\partial z} = N^2 \sin \theta \cos \theta$$

which shows that rotation increases with z , which means with latitude in the northern equatorial region, when the squared Brunt-Väisälä frequency is positive (*i.e.* with stable stratification).

Hence, compressibility changes drastically the torque. We traced this difference to the fact that, in the Boussinesq model, density is only a function of temperature and therefore isochores are identical to isotherms while in the compressible case isochores are strongly influence by pressure.

We also examined the dependence of the differential rotation with the viscosity; we find that it is independent of viscosity in the asymptotic régime $E \ll 1$. This property is also shared by the Boussinesq model which gives the explanation. As shown in Rieutord (2006), viscosity is necessary to determine the differential rotation since the inviscid case is degenerate: an arbitrary function of $r \sin \theta$ (a geostrophic flow) can always be added to u_φ . Viscosity lifts this degeneracy by “choosing” the geostrophic

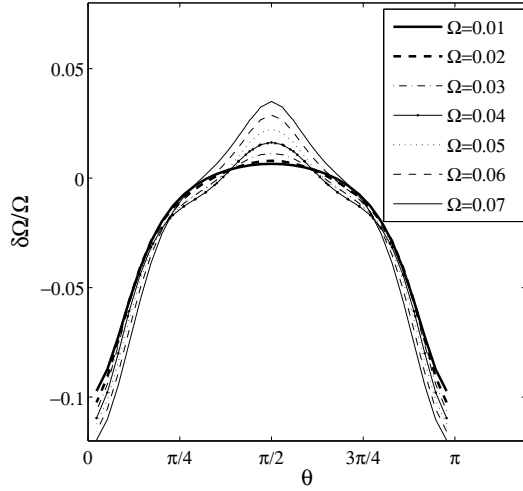


Fig. 10. Relative differential rotation on the last isobar.

flow such that no tangential stress is exerted on the outer boundary while the meridional flow exactly matches the Ekman pumping. As Ekman pumping and meridional flows are both proportional to viscosity, this quantity simplifies and we are left with a differential rotation independent of it.

Furthermore, an interesting property is shown in figure 10: except for rotations faster than $\Omega = 0.03$ ($\sim 36\%$ of the critical angular velocity), the relative surface differential rotation keeps the same profile. Poles are 10% slower than equator. If the shape of this profile is reachable through observations, a comparison to this shape will give interesting informations on the dynamical state of the fluid (presence of turbulence, magnetic fields...).

We also note from Fig. 10, that at high rotation rate, a kind of equatorial jet develops between latitude $\pm 20^\circ$. If confirmed by more realistic models, such a jet may play an important role in mass loss for stars rotating close to the breakup limit.

Finally, one may wonder whether the differential rotation is sensitive to the shape of the surface where boundary conditions are taken; in other words, what will happen when our spherical container is changed into a spheroid matching the shape of an isobar? We conjecture that not much should change for we note that while changing Ω , and thus the shape of isobars, the form of the differential rotation remains very similar.

The case of meridional circulation, displayed in Fig. 11, shows three cells of circulation. This feature of the meridional flow is controlled by the distribution of the Brunt-Väisälä frequency and the Prandtl number as shown in the Boussinesq case. As far as the turnover time associated with this circulation is concerned, we refer to the discussion in Rieutord (2006); indeed except the profile of density, there is no significant change: the turnover time remains controlled by viscosity (likely turbulent) and the Prandtl number.

Like in the Boussinesq case questions of stability, would require a full study. As in Rieutord (2006), we nevertheless have a look to the case of axisymmetric barotropic stability. We thus compute the angular momentum distribution along an isentropic surface; more precisely, we verify that along such a surface, a fluid parcel has an increasing angular momentum when its position gets farther from the rotation axis. This is a necessary condition for axisymmetric stability and Fig. 12 shows that this is indeed the case.

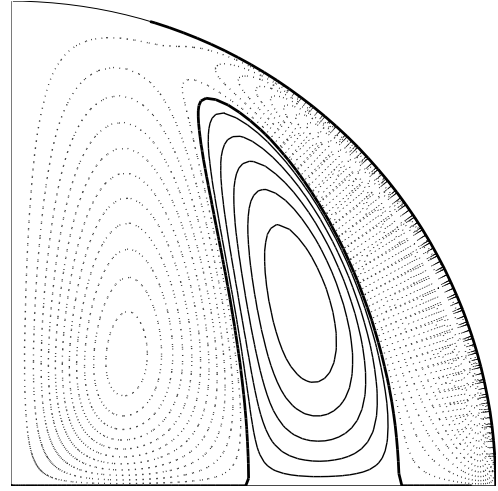


Fig. 11. Meridional circulation, solid lines represent counter-clockwise circulation and dotted clockwise circulation. $p_s = 10^{-5}$, $E = 10^{-8}$, $\Omega = 0.07$, $\alpha = 15.2$, $\sigma_T = 1.5$.

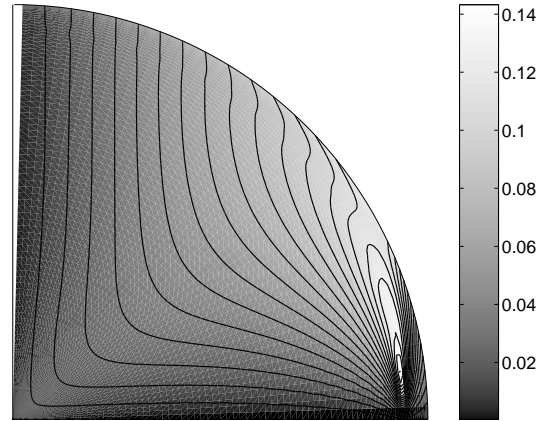


Fig. 12. Directional derivative of L_z along an equal entropy lines, *i.e.* $(\mathbf{n} \cdot \nabla)L_z$ where \mathbf{n} is a unit vector tangential to the isentropy surface and directed towards the equator.

6. Conclusions

In this paper we presented a physically self-consistent model of a rotating self-gravitating perfect gas heated by nuclear reactions and enclosed in a container with constant absorption coefficient radiating like a black body; heat transport in the gas is purely radiative, insured by a Kramers type opacity.

This is a simplified model for a completely radiative star which rotates at a significant fraction of the breakup angular velocity. We thus generalized the approach of Rieutord (2006) by taking into account more realistic properties of a stellar plasma.

Such a fluid is never in hydrostatic equilibrium and a baroclinic flow develops. Taking into account viscosity, we computed such a flow in its steady state, namely the differential rotation and the meridional circulation. Interestingly enough, the results show that equatorial regions are rotating faster than polar ones and, provided that rotation is less than $\sim 36\%$ of the breakup velocity, the surface profile $\delta\Omega/\Omega$ is independent of both viscosity and rotation rate.

Although our model is still preliminary, we had a look to the anisotropy of the emitted flux; we found that the pole/equator ratio is less contrasted than what is predicted by the von Zeipel

model. We also showed that when rotation is fast enough equatorial regions become convectively unstable.

In parallel to the construction of this model we tested, for the first time to our knowledge, the use of spectral methods in the stellar structure computations. Our first results are promising in terms of precision and robustness: we recover the precision of a finite difference type model with ten times less grid points. Such a gain in efficiency is necessary for the future computations of the evolution of a rotating star with a two-dimensional model.

The next step is of course to confirm these results using a model with coordinates adapted to the spheroidal shape of the isobars. In this case boundary conditions can be cleanly applied and the surface pressure can be decreased to very low values adapted to the matching of an atmosphere model. Of course, the inclusion of modeled convection zone is also a necessary step for the completeness of models to be used in the interpretation of observations.

Acknowledgements. We thank Bernard Pichon for providing us with 1D models from CESAM code and for many helpful discussions. This work is part of the ESTER project aimed at modeling stars in two dimensions; it is supported by the Programme National de Physique Stellaire along with the Action Spécifique pour la Simulation Numérique en Astrophysique. FE thanks the CNRS postdoctoral programme for its support during his stay at LATT in Toulouse.

References

- Aufdenberg, J. P., Mérand, A., Coudé du Foresto, V., et al. 2006, *ApJ*, 645, 664
 Bonazzola, S., Gourgoulhon, E., & Marck, J.-A. 1998, *Phys. Rev. D*, 58, 104020
 Bonazzola, S., Gourgoulhon, E., & Marck, J.-A. 1999, *J. Computational and Applied Math.*, 109, 433
 Canuto, C., Hussaini, M. Y., Quarteroni, A., & Zang, T. A. 2006, *Spectral Methods: Fundamentals in Single Domains* (Springer Verlag)
 Christensen-Dalsgaard, J. & Reiter, J. 1995, in *ASP Conf. Ser. 76: GONG 1994. Helio- and Astro-Seismology from the Earth and Space*, ed. R. K. Ulrich, E. J. Rhodes, Jr., & W. Dappen, 136–+
 Dintrans, B. & Rieutord, M. 2000, *A & A*, 354, 86
 Domiciano de Souza, A., Kervella, P., Jankov, S., et al. 2005, *A & A*, 442, 567
 Domiciano de Souza, A., Vakili, F., Jankov, S., Janot-Pacheco, E., & Abe, L. 2002, *A&A*, 393, 345
 Eriguchi, Y. & Müller, E. 1985, *A&A*, 146, 260
 Fornberg, B. 1998, *A practical guide to pseudospectral methods* (Cambridge University Press)
 Grandclément, P. 2006, in *Stellar fluid dynamics and numerical simulations: from the Sun to neutron stars*, ed. M. Rieutord & B. Dubrulle (EDP Sciences), 153–180
 Jackson, S., MacGregor, K. B., & Skumanich, A. 2005, *Astrophys. J. Supp. Ser.*, 156, 245
 Kervella, P. & Domiciano de Souza, A. 2006, *A&A*, 453, 1059
 McAlister, H. A., ten Brummelaar, T. A., Gies, D. R., et al. 2005, *ApJ*, 628, 439
 Morel, P. 1997, *A & A Suppl. Ser.*, 124, 597
 Ostriker, J. P. & Bodenheimer, P. 1968, *ApJ*, 151, 1089
 Peterson, D., Hummel, C., Pauls, T., et al. 2006a, *ApJ*, 636, 1087
 Peterson, D. M., Hummel, C. A., Pauls, T. A., et al. 2006b, *Nature*, 440, 896
 Peyret, R. 2002, *Spectral methods for incompressible viscous flow* (New-York: Springer)
 Reese, D., Lignières, F., & Rieutord, M. 2006, *A & A*, 455, 621
 Rieutord, M. 1987, *Geophys. Astrophys. Fluid Dyn.*, 39, 163
 Rieutord, M. 2006, *A & A*, 451, 1025
 Roxburgh, I. W. 2004, *A & A*, 428, 171
 Uryu, K. & Eriguchi, Y. 1994, *MNRAS*, 269, 24
 Uryu, K. & Eriguchi, Y. 1995, *MNRAS*, 277, 1411
 Valdettaro, L., Rieutord, M., Braconnier, T., & Fraysse, V. 2006, to appear in *J. Comput. and Applied Math.*, physics/0604219, 1
 Zahn, J.-P. 1992, *A & A*, 265, 115
 Zorec, J., Domiciano de Souza, A., Frémat, Y., & Vakili, F. 2005, in *SF2A-2005: Semaine de l’Astrophysique Française*, ed. F. Casoli, T. Contini, J. M. Hameury, & L. Pagani, 363–+